Journal of Materials Chemistry C

RSC Publishing

PAPER

View Article Online
View Journal | View Issue

Cite this: J. Mater. Chem. C, 2013, 1, 4114

On the origin of enhanced thermoelectricity in Fe doped $Ca_3Co_4O_9$

Tao Wu,[a] Trevor A. Tyson,*[a] Jianming Bai,[b] Kaumudi Pandya,[c] Cherno Jaye[d] and Daniel Fischer[d]

Received 14th March 2013
Accepted 13th May 2013

DOI: 10.1039/c3tc30481g

www.rsc.org/MaterialsC

Resistivity and Seebeck coefficient measurements on $Ca_3Co_{4-x}Fe_xO_9$ ($x = 0$, 0.05, 0.1, 0.2 and 0.25) reveal enhanced thermoelectric performance with an optimal x value of 0.2. X-ray diffraction measurements show continuous Fe doping into the host lattice, while X-ray absorption experiments reveal that Fe substitutes for Co in the Ca_2CoO_3 (rock salt) block. The Fe substitution for Co produces electron doping. The local structure around Fe in the Ca_2CoO_3 block becomes disordered, while the structure in the conducting CoO_2 layer becomes more ordered. The structural change in the CoO_2 layer plays the key role to enhance the electron transport. The highest ordered structure is achieved at $x = 0.2$ with the lowest resistivity. Soft X-ray absorption measurements find no Co site spin-state change with Fe doping. Thermoelectric property enhancement associated with doping induced structural change points to a new approach for creating materials with improved ZT in complex oxide systems.

Introduction

Thermoelectric materials are promising renewable energy materials as they convert heat to electrical power directly and *vice versa*. It is of great importance for waste energy recovering and cooling.[1] The efficiency of a thermoelectric material is defined as $ZT = S^2T\rho^{-1}\kappa^{-1}$, where ZT is dimensionless figure of merit, S is Seebeck coefficient, ρ is electrical resistivity and κ is thermal conductivity. The power factor can be expressed by $P = S^2\rho^{-1}$, with ZT then given by $PT\kappa^{-1}$. ZT $\sim$ 3 is a critical value to make thermoelectric materials comparable to the conventional compressor-type refrigerator in cooling. The highest ZT in bulk material up to now was reported to be 2.2 at 915 K recently.[2]

Layered cobaltite has been attracted much interest as promising thermoelectric materials after the discovery of $NaCo_2O_4$ (ref. 3) with high power factor. Other advantages of oxide-based thermoelectric materials include environmental friendliness and high chemical and thermal stability at high temperatures. In this class, the cobaltite $[Ca_2CoO_3]_{0.62}[CoO_2]$, known as $Ca_3Co_4O_9$, with incommensurate misfit structure has been widely investigated. ZT of single crystal $Ca_3Co_4O_9$ was reported to be $\sim$1 at 1000 K.[4] Thus it is considered to be a promising p-type thermoelectric material.[5] The structure of $Ca_3Co_4O_9$ is different from the standard thermoelectrics, such as PbTe or Bi_2Te_3. It is a complex incommensurate monoclinic misfit structure with the super space group $X2/m(0b0)s0$. It consists of two interpenetrating subsystems of a triple-layered NaCl-type rock salt Ca_2CoO_3 block (subsystem 1) and a CdI_2-type hexagonal CoO_2 layer (subsystem 2)[6–10] (see Fig. 1). The subsystems stack along the c axis and share the same a, c and β lattice parameters: a = 4.8270(5) Å, c = 10.8300(2) Å, $\beta = 98.136(1)^\circ$. The mismatch of the unit cells along the b axis results in different b lattice parameters for each subsystem: $b_1 = 4.5615(2)$ Å (subsystem 1) and $b_2 = 2.8173(1)$ Å (subsystem 2).[10] The CoO_2 layer is conducting and the insulating Ca_2CoO_3 block is regarded as a charge reservoir.[11]

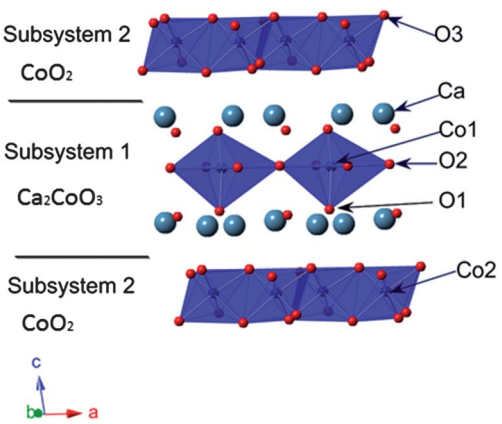

Fig. 1 The crystal structure of $Ca_3Co_4O_9$ shows the Ca_2CoO_3 block (subsystem 1) and CoO_2 layer (subsystem 2) with details of the CoO_6 octahedra in each subsystem.

[a]Department of Physics, New Jersey Institute of Technology, Newark, NJ 07102, USA. E-mail: tyson@njit.edu

[b]National Synchrotron Light Source, Brookhaven National Laboratory, Upton, NY 11973, USA

[c]SAIC, Brookhaven National Laboratory, Upton, NY 11973, USA

[d]Materials Science and Engineering Laboratory, National Institute of Standards and Technology, Gaithersburg, MD 20899, USA

Previous work focused on enhancing the thermoelectric properties of $Ca_3Co_4O_9$, including various preparations (as powders, crystals and thin films)[4,12–23] in addition to chemical doping.[14,24–31] Some doping systems were investigated in all the forms as well, such as the Bi doped $Ca_3Co_4O_9$.[32–34] However, the mechanism of the thermoelectric property enhancement was not understood well.

In this work, we focus on the Fe doped $Ca_3Co_4O_9$ bulk system. $Ca_3Co_4O_9$ doping with Fe was claimed to possess the best thermoelectric performance (highest ZT) compared to Cu and Mn doped materials.[24] The simultaneous increase of S and decrease of ρ were attributed to the strong electronic correlation with larger electronic specific heat coefficient γ and Fermi liquid transport coefficient A and smaller Fermi liquid to incoherent metal transition temperature T^* for the Fe doped $Ca_3Co_4O_9$. It was argued that Fe occupied the Co site in CoO_2 layer. Recently, thermoelectric properties of $Ca_3Co_{3.8}M_{0.2}O_9$ (M = Co, Cr, Fe, Ni, Cu and Zn) were investigated and the Fe doped system was claimed to have the highest ZT. It was also reported that Fe^{2+}/Fe^{3+} ion substitute for the Co^{3+}/Co^{4+} ions in the CoO_2 layer and the difference of the valence states results in a carrier concentration increase.[35] Thermoelectric properties of Fe doped $Ca_3Co_4O_9$ as a function of doping level ($Ca_3Co_{4-x}Fe_xO_9$ ($x = 0$, 0.05, 0.1 and 0.2)) were measured and $x = 0.05$ was found as the optimal doping level. The enhancement of the thermoelectric properties was claimed to be induced by the increase of carrier concentration.[36] The same group also conducted X-ray absorption near-edge structure (XANES) measurements on Co K-edge and $L_{2,3}$-edge and O K-edge for $Ca_3Co_{4-x}Fe_xO_9$ ($x = 0$, 0.05, 0.1 and 0.15). By integrating the absorption intensity, it was suggested the amount of unoccupied Co 3d state has the same trend with the resistivity and the carrier concentration is associated with the oxygen content in the sample. Maximum carrier concentration was found at $x = 0.05$.[37]

Although previous work concluded that doping with Fe improves the thermoelectric properties of $Ca_3Co_4O_9$, the structural origin of the thermoelectric property enhancement by Fe doping was not understood and has not been sufficiently investigated. In addition, no previous study combined both detailed structural studies as well as thermoelectric measurements on the same samples. It is of great importance to understand the changes related to the thermoelectric property increase with Fe doping, including (1) atomic site location of the Fe dopant, (2) concomitant structural changes, (3) how does the structural change affect the thermoelectric properties and (4) the nature of any spin-state contribution to the transport properties change.

In this work, a series of Fe doped $Ca_3Co_4O_9$ samples ($Ca_3Co_{4-x}Fe_xO_9$ ($x = 0$, 0.05, 0.1, 0.2 and 0.25)) were prepared. Temperature dependent thermoelectric properties, including electrical resistivity and Seebeck coefficient, were measured and power factor was calculated. Room temperature carrier concentrations were determined by Hall measurements. Both synchrotron powder X-ray diffraction (XRD) and X-ray absorption spectroscopy (XAS) were conducted to explore the structural change as a function of Fe doping and its impact on the thermoelectric properties. XANES measurements for Co $L_{2,3}$-edge and O K-edge were performed as well to investigate the electronic structure and spin-state changes with Fe doping. We found that Fe atoms substitute Co1 in the Ca_2CoO_3 block. Doping with Fe modifies both subsystems with the CoO_2 layer becoming more ordered. Carrier concentration is determined by both the oxygen content and electron doping with increasing Fe. The competition between carrier concentration and mobility (structure) change induced by Fe doping results in the lowest resistivity at $x = 0.2$. No significant spin-state change was found with Fe doping and the structural change dominates the thermoelectric properties enhancement.

Experimental methods

Single-phase polycrystalline $Ca_3Co_{4-x}Fe_xO_9$ ($x = 0$, 0.05, 0.1, 0.2 and 0.25) were prepared by solid state reaction. Stoichiometric amounts of high purity (99.9%) $CaCO_3$, Co_3O_4 and Fe_2O_3 were ground, mixed thoroughly and calcined at 900 °C in air for 24 hours. The mixture was reground and pressed into pellets. The pellets were heated at 920 °C in air for 24 hours. The latter step was repeated and the final pellets were annealed at 750 °C in flowing oxygen for 36 hours. The density of all the samples was measured by an Ultrapyc 1200e. Resistivity and Seebeck coefficient measurements for all the samples up to 315 K were carried out with a Physical Property Measurement System (PPMS, Quantum Design). Room temperature Hall measurements were conducted sweeping magnetic field from −8 T to 8 T with PPMS as well. Synchrotron powder XRD measurements on all the samples were conducted at beamline X14A at National Synchrotron Light Source (NSLS), Brookhaven National Laboratory (BNL) using a high count rate linear detector. The X-ray wavelength was 0.77831 Å and the resolution in 2θ was 0.005°. Finely ground $Ca_3Co_{4-x}Fe_xO_9$ powder (<25 μm) was loaded into a glass capillary with an inner diameter 0.5 mm. Rietveld refinements were performed on the XRD data using JANA 2006.[38]

X-ray absorption spectra for Co K-edge and Fe K-edge for $Ca_3Co_{4-x}Fe_xO_9$ were collected at beamline X11B at NSLS, BNL. The samples were prepared by grinding and sieving the powder (500 mesh) and brushing it onto Kapton tape. Co and Fe foils were utilized to calibrate the energy for each edge measurements. Measurements were made in Fluorescence mode for Fe K-edge and transmission mode for Co K-edge. The reduction of X-ray absorption fine-structure (XAFS) data was performed by standard procedure.[39,40] Data analysis was carried out as in ref. 41. Co K-edge data over the k-range $2.8 < k < 13.3$ Å^{-1} was used and fits in R space were carried out over the range $0.9 < R < 3.1$ Å. The k-range used for Fe K-edge was $2.6 < k < 9.5$ Å^{-1} (the upper limit on the k-range was constrained by the presence of the Co K-edge) and the R-range was $0.9 < R < 3.4$ Å for fitting. S_0^2 was fixed to 0.86 and 0.8 for Co and Fe K-edge fitting, respectively. Co $L_{2,3}$-edge and O K-edge XANES spectra for $Ca_3Co_4O_9$ and $Ca_3Co_{3.8}Fe_{0.2}O_9$ were conducted at the National Institute of Standards and Technology (NIST) soft X-ray beamline U7A at NSLS, BNL.

Results and discussion

The density of all the samples is similar and the value is 4.45 ± 0.16 g cm^{-3} which is 95% of the theoretical density of 4.68 g cm^{-3}

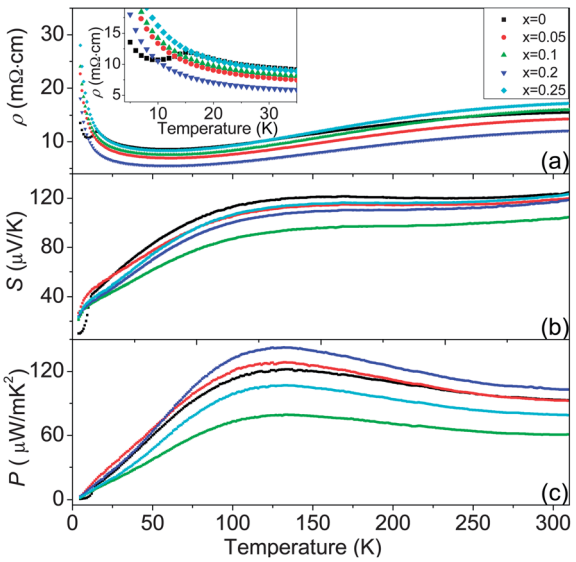

Fig. 2 Temperature dependent resistivity (a), Seebeck coefficient (b) and power factor (c) of $Ca_3Co_{4-x}Fe_xO_9$ ($x = 0$, 0.05, 0.1, 0.2 and 0.25). The inset in (a) shows that the resistivity anomaly in $Ca_3Co_4O_9$ near 27 K disappears with Fe doping.

(ref. 6) indicating that the pellet samples were well compressed. Temperature dependent resistivity and Seebeck coefficient of $Ca_3Co_{4-x}Fe_xO_9$ ($x = 0$, 0.05, 0.1, 0.2 and 0.25) are shown in Fig. 2(a) and (b). Fig. 2(c) is the calculated power factor. The inset in Fig. 2(a) shows the resistivity anomaly near 27 K associated with a magnetic transition[42] in $Ca_3Co_4O_9$ which is also found in our previous work.[43] This feature is suppressed by Fe doping. With respect to the over all shape, doping with Fe does not change the overall shape of the ρ–T and S–T curves, while the magnitude of resistivity and Seebeck coefficient changes with Fe doping. $x = 0.2$ has the lowest resistivity and relatively high Seebeck coefficient which results in a 11% increase of power factor at room temperature. Thus $x = 0.2$ is the optimal doping level.

Fig. 3 presents the carrier concentration (n) of Fe doped $Ca_3Co_4O_9$ as a function of doping level. The undoped $Ca_3Co_4O_9$ has the n value $(2.32 \pm 0.28) \times 10^{20}$ cm^{-3} and it increases at low doping levels following with a drop above $x = 0.1$. It was reported that the n value for the undoped $Ca_3Co_4O_9$ is significantly lower than the values for the Fe doped ones.[37] Considering the geometrical errors, the Fe doped samples may have approximately the same value of n. It should be noted that both the magnitude and the trend of n in this work are consistent with the reference mentioned before. It was suggested that the oxygen content change induced by doping is responsible for the carrier concentration change.[37,44] Detailed oxygen content change as a function of Fe doping and the effects on the thermoelectric properties will be studied in the future. However this is not the complete picture. Carrier concentration is also determined by the electron doping as a result of significant decrease of n at higher Fe doping levels ($x = 0.2$ and 0.25) (see discussion below). In this work, we focus on the structural change induced by Fe doping to explore the origin of the thermoelectric properties enhancement with Fe doping, especially the electrical transport property. Structural measurements as a function of Fe doping, including synchrotron XRD and XAS, were performed.

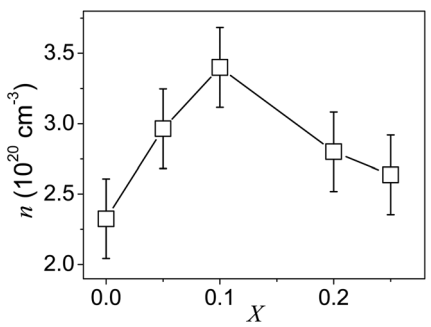

Fig. 3 Fe doping dependent carrier concentration (n) of $Ca_3Co_{4-x}Fe_xO_9$ ($x = 0$, 0.05, 0.1, 0.2 and 0.25) at room temperature.

Fig. 4(a) shows the synchrotron XRD patterns of $Ca_3Co_{4-x}Fe_xO_9$ ($x = 0$, 0.05, 0.1, 0.2 and 0.25) at room temperature. Single-phase was confirmed for all the members. The broad rise at low 2θ angle is the background from the glass capillary. The diffraction peak (0040) shifts systematically to lower angle with Fe doping in the inset of Fig. 4(a). It indicates the dopant Fe enters into the $Ca_3Co_4O_9$ lattice and the corresponding lattice parameters are expanded systematically. Rietveld refinement of synchrotron XRD data for $Ca_3Co_{3.8}Fe_{0.2}O_9$ at room temperature is shown in Fig. 4(b). The super space group $X2/m(0b0)s0$ was employed for the refinement.[44] Three structural models were utilized to refine the $Ca_3Co_{3.8}Fe_{0.2}O_9$ XRD data: (1) $Ca_3Co_4O_9$

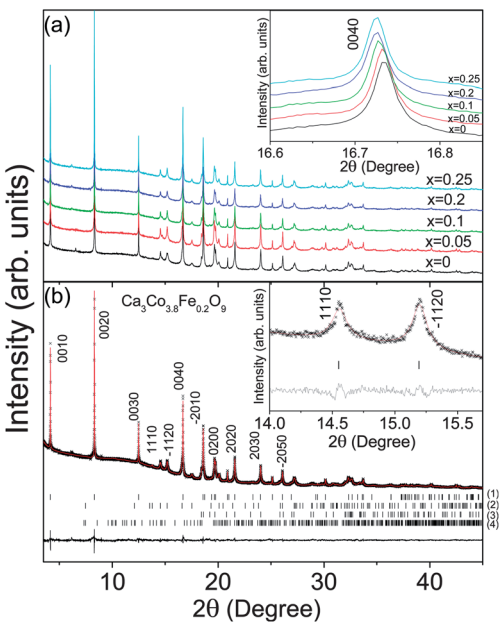

Fig. 4 (a) Synchrotron powder XRD patterns of $Ca_3Co_{4-x}Fe_xO_9$ ($x = 0$, 0.05, 0.1, 0.2 and 0.25). The broad rise at low 2θ angle is the background from the glass capillary. The inset in (a) shows the details of peak (0040) shift with Fe doping. (b) Rietveld refinement of XRD on $Ca_3Co_{3.8}Fe_{0.2}O_9$. The observed (crosses), calculated (solid line) and difference (bottom line) profiles are shown. The bars show the peak positions of reflections common to both subsystems (1), reflections of subsystem 1 (2), reflections of subsystem 2 (3) and satellite reflections (4). The inset shows the details of the Rietveld refinement for two specific peaks.

model, (2) $Ca_3Co_4O_9$ model with Fe atoms in the Co1 site in Ca_2CoO_3 block and (3) $Ca_3Co_4O_9$ model with Fe atoms in the Co2 site in CoO_2 layer. The weighted profile R factor (R_{wp}) for each model was 0.0234, 0.0234 and 0.0235, respectively. Structural parameters obtained from these three models are the same within experimental errors. Other doping level samples have the same results as $x = 0.2$. This result is not surprised because the difference of the atomic number between Co and Fe is only one and it is hard to be distinguished by X-ray scattering if Fe enters into a Co site. Moreover, only small fractions of the Co atoms are replaced by Fe atoms. Here the second model (Fe substitute for Co1) is used to show the Rietveld refinement results for all the doping samples since it is shown that Fe atoms enter into the Co1 sites in Ca_2CoO_3 block by XAFS measurements. Details will be discussed below. The observed (crosses), calculated (solid line) and difference (bottom line) profiles are shown in Fig. 4(b). The vertical bars display the peak positions of reflections common to both subsystems (1), reflections of subsystem 1 (2), reflections of subsystem 2 (3) and satellite reflections (4), respectively. The inset in Fig. 4(b) shows the details of the Rietveld refinement for specific peaks. Note that splitting of the peak (−1120) is found in $Ca_3Co_4O_9$ and it was also observed by other ref. 10 and 43. However, it disappears for the Fe doped samples. It indicates the long-range structure becomes more symmetric with Fe doping. Fig. 1 shows the crystal structure of $Ca_3Co_4O_9$. The Ca_2CoO_3 block (subsystem 1) and CoO_2 layer (subsystem 2) are shown as well as the detail of the CoO_6 octahedra in both subsystems.

Fig. 5(a–d) give the lattice parameters a, c, b_1 and b_2 as a function of Fe doping. Both lattice parameters a and c (Fig. 5(a) and (b)) increase linearly with Fe doping up to $x = 0.2$ and follow with saturation and slight decrease at $x = 0.25$. The lattice parameter b_1 (Fig. 5(c)) increases at low doping level $x = 0.05$ followed by a sudden drop at $x = 0.1$. It then generally decreases to the minimum at $x = 0.2$ and goes up again at $x = 0.25$. In Fig. 5(d), b_2 slightly drops at $x = 0.05$ and keeps the value to $x = 0.1$. A sudden decrease occurs at $x = 0.2$ following with a constant to $x = 0.25$. Note that all the panels in Fig. 5 have the same vertical scale. The lattice parameters change with doping suggests that Fe atoms enter into the $Ca_3Co_4O_9$ lattice at Co sites. However, the specific location of the Fe dopants (replacing either Co1 or Co2) is not evident. Although lattice parameters a and c have the largest change with Fe doping, it is difficult to locate the Fe atoms because a and c are common to both subsystems. b_1 and b_2 correspond to each subsystem, but both of them change a similar magnitude with Fe doping.

In order to determine the position of the doped Fe ions relative to the Co sites in the subsystems, we carried out X-ray absorption measurements at the Co and Fe K-edges. A simulation of the Co K-edge XAFS structure function for the Co1 (Ca_2CoO_3 block) and Co2 (CoO_2 layer) sites is given in Fig. 6(a) for comparing with the measurements. The Ca_2CoO_3 and CoO_2 structural models from ref. 8 were used to generate the FEFF files at Co site and a global σ^2 was set to 0.008 Å^2. The first shell in both subsystems corresponds

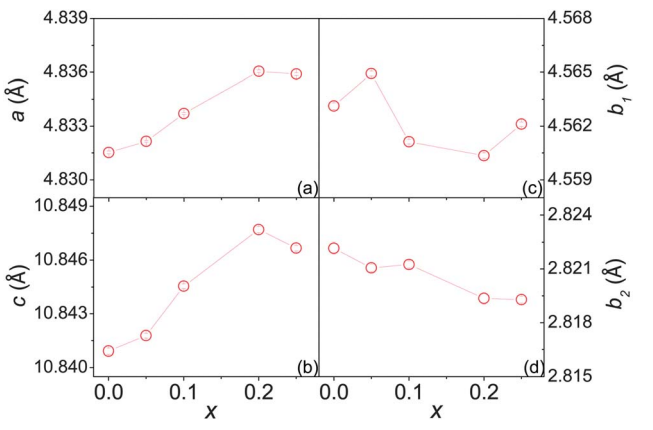

Fig. 5 Lattice parameters a (a), c (b), b_1 (c) and b_2 (d) of $Ca_3Co_{4-x}Fe_xO_9$ as a function of Fe doping. All panels have the same vertical scale.

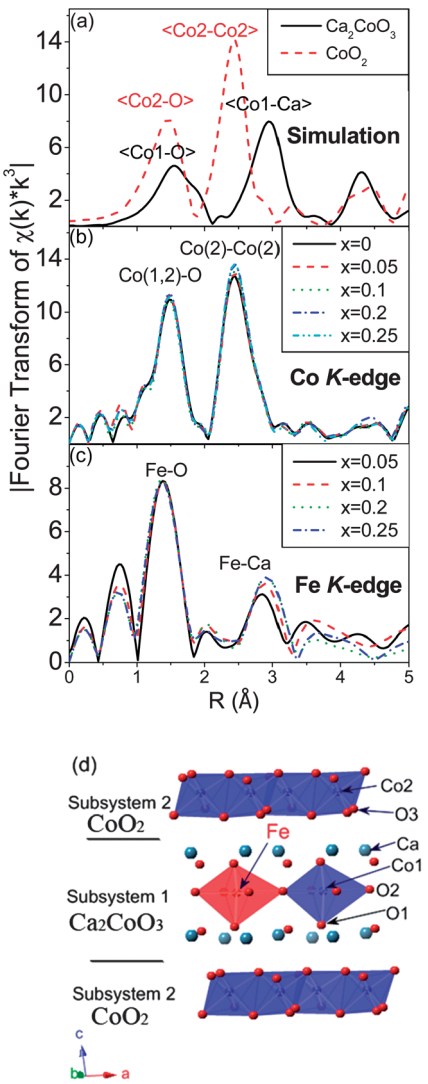

Fig. 6 Simulated XAFS structure functions for Co sites in each subsystem (Ca_2CoO_3 and CoO_2) in (a). XAFS structure functions for average Co sites of $Ca_3Co_{4-x}Fe_xO_9$ (x = 0, 0.05, 0.1, 0.2 and 0.25) in (b), and average Fe sites of $Ca_3Co_{4-x}Fe_xO_9$ (x = 0.05, 0.1, 0.2 and 0.25) in (c). Note that the position of the second shell for Fe site in (c) indicates Fe atoms substitute for Co1 in Ca_2CoO_3 block. (d) Schematic of the crystal structure for Fe doped $Ca_3Co_4O_9$ with Fe atoms in the Co1 site in Ca_2CoO_3 block. Note that the structure in (d) does not mean the real Fe content. The ratio of Co1 to Fe for $Ca_3Co_{3.8}Fe_{0.2}O_9$ is approximately 7 : 1.

to Co–O bonds. The second shell in Ca_2CoO_3 is Co1–Ca bond and it corresponds to Co2–Co2 bond in CoO_2. Obvious shifts in the second shell for each subsystem can be observed due to the distinctly different higher shell coordination. This will enable us to determine the location of the Fe dopants. In other words, the location of the second shell in the XAFS structure function for Fe K-edge determines the Fe position. If it is in the same R as the ⟨Co2–Co2⟩ peak in Fig. 6(a), Fe atoms enter into the Co2 sites in CoO_2 layer. Otherwise, Fe substitutes for Co1 in Ca_2CoO_3 block if it locates at the same position as ⟨Co1–Ca⟩ shell. A direct comparison of the Fe K-edge and Co K-edge spectra can be made since the atomic numbers are close.

The XAFS structure functions of Co K-edge and Fe K-edge for the Fe doped $Ca_3Co_4O_9$ are shown in Fig. 6(b) and (c). No significant change is observed for the oxygen shell in both Co and Fe sites. The magnitude of the second shell corresponding to the Co2–Co2 bond in Fig. 6(b) increases continuously with Fe doping up to $x = 0.2$ and it saturates at $x = 0.25$. It indicates enhanced structural order around the Co2 sites with Fe doping. No significant shift occurs for the peak position with Fe doping. The second shell about Fe (Fig. 6(c)) is at more distant than Co2–Co2 bond in the CoO_2 layer. It matches well to the model for the Co1–Ca shell in Fig. 6(a). This result strongly supports a model for Fe atoms substituting for Co1 in Ca_2CoO_3 subsystem exclusively up to the highest doping level studied ($x = 0.25$). The magnitude of the second shell in Fig. 6(c) increases and the peak position shifts to high R with Fe doping up to $x = 0.2$ and it saturates at $x = 0.25$. Although the peak grows with Fe doping, the local structure near Fe is disordered. Details will be discussed below. Fig. 6(d) gives a schematic of the crystal structure for Fe doped $Ca_3Co_4O_9$ with the Fe atom in the Co1 site. Note that the purpose of Fig. 6(d) is to show the Fe position but not the accurate content. The analysis indicates that the ratio of Co1 to Fe for $Ca_3Co_{3.8}Fe_{0.2}O_9$ is approximately 7 : 1.

The valence state of Fe was also determined. Fig. 7(a) shows the Fe K-edge XANES spectra of $Ca_3Co_{4-x}Fe_xO_9$ ($x = 0.05, 0.1, 0.2$ and 0.25). No significant edge shift occurs with Fe doping. Furthermore, the Fe K-edge XANES spectrum of $Ca_3Co_{3.8}Fe_{0.2}O_9$ is compared to a series of standard compounds[45] with 2+, 3+, and 4+ valence states in Fig. 7(b). It is clear that the spectrum of $Ca_3Co_{3.8}Fe_{0.2}O_9$ (thick line) falls into the group of Fe^{3+} standards. XAS studies found that the valence state of Co1 in Ca_2CoO_3 block should be close to 2+.[6,46] This result is also confirmed by the Co K-edge XANES spectra in this work and it will be discussed below. Thus, substitution of Co1 with Fe produces electron doping. However, the oxygen content change induced by Fe doping may dominate the carrier concentration change at low doping level. In other words, Fe doping changes the oxygen content and it indirectly adjusts the carrier concentration at low doping levels. Electron doping becomes more important at higher doping levels resulting in the carrier concentration drop for p-type $Ca_3Co_4O_9$. Fig. 7(c) gives the Co K-edge XANES spectra of $Ca_3Co_4O_9$ and $Ca_3Co_{3.8}Fe_{0.2}O_9$. Two independent data sets for each sample were included to show the high data quality with good statistics. No edge shift was observed indicating that the average valence state of Co does not change with Fe doping. The expanded white line region was shown in the inset of Fig. 7(c). The curves for the same doping level overlap very well. It is obviously $x = 0.2$ has a larger amplitude. This amplitude increase in the XANES spectrum indicates a higher ordered structure around the Co site with Fe doping. Moreover, Co K-edge XANES spectrum gives the average structural information from both Co1 and Co2 sites. The Co1 layer is known to be disordered with Fe doping (see below). Thus the conducting Co2 layer is even more significantly ordered.

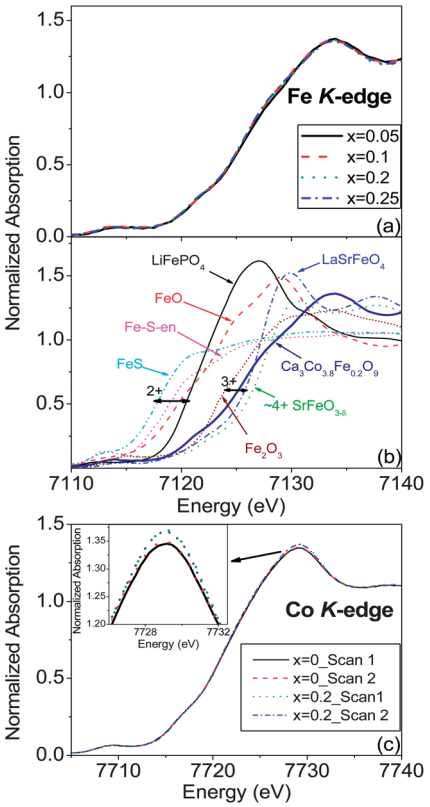

Fig. 7 (a) Fe K-edge XANES spectra of $Ca_3Co_{4-x}Fe_xO_9$ ($x = 0.05, 0.1, 0.2$ and 0.25). (b) Fe K-edge XANES spectrum of $Ca_3Co_{3.8}Fe_{0.2}O_9$ (thick line) compared to Fe systems of 2+, 3+, and 4+ valence states. Note that the spectrum $Ca_3Co_{3.8}Fe_{0.2}O_9$ is obviously in the group of Fe 3+ range. (c) Co K-edge XANES spectra of $Ca_3Co_{4-x}Fe_xO_9$ ($x = 0$ and 0.2). The inset shows the expanded white line region indicating a more ordered structure around Co site in $Ca_3Co_{3.8}Fe_{0.2}O_9$.

In order to understand the local structural change of $Ca_3Co_4O_9$ with Fe doping quantitatively, structural refinement of Co K-edge and Fe K-edge XAFS data was conducted. Fig. 8(a) and (b) show the fits of the Fourier transform of the Co and Fe K-edges XAFS data for $Ca_3Co_{3.8}Fe_{0.2}O_9$. The dash lines show typical model curves which match with the data well. Other samples have the same fitting quality. Table 1 lists the extracted bond distances of $Ca_3Co_4O_9$ and $Ca_3Co_{3.8}Fe_{0.2}O_9$ from XAFS data. Doping with Fe does not change ⟨Co–O⟩ and ⟨Co2–Co2⟩ distances much which means the local structure is not significantly modified by Fe doping. ⟨Co–O⟩ bond consists of ⟨Co1–O⟩ and ⟨Co2–O⟩ bonds and the former one is longer as shown in Fig. 6(a). ⟨Fe–O⟩ distance is ~0.05 Å shorter than ⟨Co–O⟩ distance and it is even much shorter than ⟨Co1–O⟩ distance. For comparison, ⟨Co^{2+}–O⟩ and ⟨Fe^{3+}–O⟩ distances are found to be 2.133 Å and 2.031 Å for CoO and Fe_2O_3 with ~0.1 Å

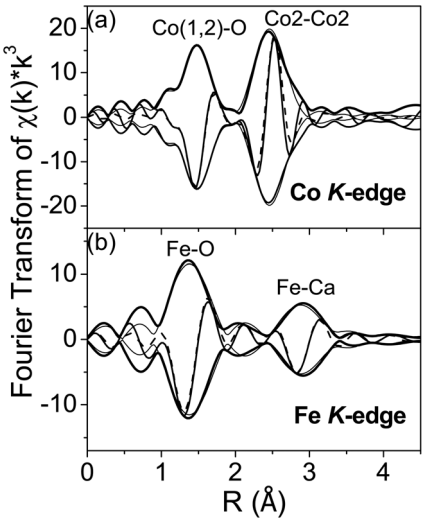

Fig. 8 Fourier transform of the Co (a) and Fe (b) K-edges XAFS data for $Ca_3Co_{3.8}Fe_{0.2}O_9$. The thin dash lines are the fits to the data.

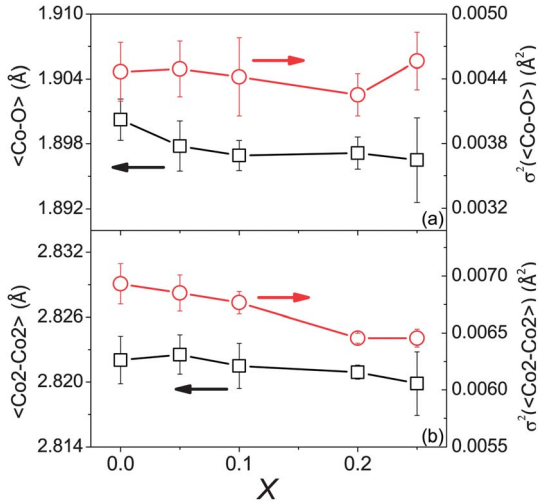

Fig. 9 Fe doping dependent bond distance ⟨Co–O⟩ and bond correlation $\sigma^2(\langle Co–O\rangle)$ (a) and bond distance ⟨Co2–Co2⟩ and bond correlation $\sigma^2(\langle Co2–Co2\rangle)$ (b) derived from Co K-edge XAFS measurements.

Table 1 Bond distances in $Ca_3Co_4O_9$ and $Ca_3Co_{3.8}Fe_{0.2}O_9$ from XAFS. For comparison, ⟨Co–O⟩ and ⟨Fe–O⟩ distances in CoO and Fe_2O_3 are also shown

$Ca_3Co_4O_9$	Co K-edge	
	⟨Co–O⟩ (Å)	1.900(2)
	⟨Co2–Co2⟩ (Å)	2.822(2)
$Ca_3Co_{3.8}Fe_{0.2}O_9$	Co K-edge	
	⟨Co–O⟩ (Å)	1.897(1)
	⟨Co2–Co2⟩ (Å)	2.821(1)
	Fe K-edge	
	⟨Fe–O⟩ (Å)	1.851(8)
	⟨Fe–Ca⟩[a] (Å)	3.034(7)
	⟨Fe–Ca⟩[b] (Å)	3.289(7)
CoO	⟨Co–O⟩ (Å)	2.133
Fe_2O_3	⟨Fe–O⟩ (Å)	2.031

[a] Fe–Ca shell 1 includes two Fe–Ca bonds. [b] Fe–Ca shell 2 includes six Fe–Ca bonds.

difference.[47,48] Hence, a higher valence state of Fe results in a shorter ⟨Fe–O⟩ bond. On the other hand, it is confirmed the valence state for Co1 is close to 2+. Note that a two-shell fit was used for the Fe–Ca distribution in the Fe K-edge XAFS structure function with two and six Fe–Ca bonds, respectively. The average bond distances of each shell are shown in Table 1.

The square symbols in Fig. 9(a) and (b) are the average bond distances of Co–O and Co2–Co2 corresponding to the first and second shell in the XAFS structure function of Co K-edge. No obvious change is observed for ⟨Co–O⟩ and ⟨Co2–Co2⟩ distances with Fe doping. Fig. 9(a) and (b) also show the bond correlation ("Debye–Waller" factor, $\sigma^2 = \langle(r - \langle r\rangle)^2\rangle$) for Co–O and Co2–Co2 bonds (circle symbols) as a function of Fe doping, respectively. No significant change occurs in $\sigma^2(\langle Co–O\rangle)$. However, $\sigma^2(\langle Co2–Co2\rangle)$ systematically decreases with Fe doping and a significant drop occurs at $x = 0.2$ following with a saturation at $x = 0.25$. Combining the Co K-edge XANES spectra in Fig. 7(c), it indicates an enhanced structural order around the Co2 sites, thus more ordered structure in the conducting CoO_2 layer with Fe doping.

Fig. 10 gives the refined bond distances and bond correlations from the Fe K-edge XAFS structure function. Fig. 10(a) shows ⟨Fe–O⟩ distance (square symbols) and $\sigma^2(\langle Fe–O\rangle)$ (circle symbols) as a function of Fe doping. No obvious change is observed for ⟨Fe–O⟩ distance and $\sigma^2(\langle Fe–O\rangle)$ with Fe doping. Fig. 10(b) and (c) are the ⟨Fe–Ca⟩ distances (square symbols) and $\sigma^2(\langle Fe–Ca\rangle)$ (circle symbols) corresponding to the two Fe–Ca shells. Although the error bar is large in Fig. 10(b) and (c), there is an apparent trend since the data sets are independent. ⟨Fe–Ca⟩ distance for both shells increases with Fe doping up to

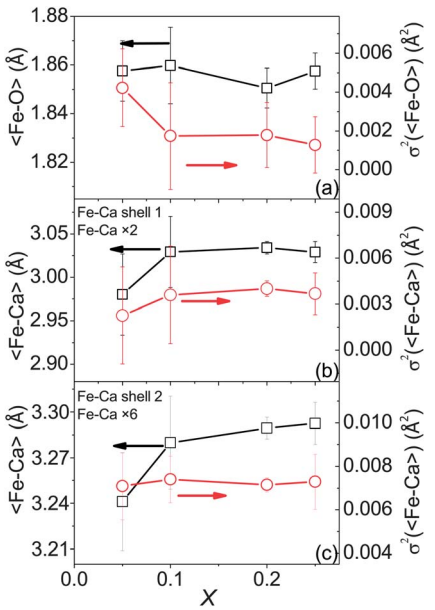

Fig. 10 Fe doping dependence of bond distance ⟨Fe–O⟩ and bond correlation $\sigma^2(\langle Fe–O\rangle)$ (a) and bond distance ⟨Fe–Ca⟩ and bond correlation $\sigma^2(\langle Fe–Ca\rangle)$ (b) and (c) derived from Fe K-edge XAFS measurements. Note that two Fe–Ca shells were used for the Fe–Ca distribution of bonds.

$x = 0.2$ and it saturates at $x = 0.25$. $\sigma^2(\langle$Fe–Ca$\rangle)$ for shell 1 (Fig. 10(b)) increases continuously up to $x = 0.2$ and it saturates at $x = 0.25$. The shorter Fe–Ca bond becomes disordered with higher Fe doping. While $\sigma^2(\langle$Fe–Ca$\rangle)$ for shell 2 is constant for the whole doping range in Fig. 10(c). Thus the local structure around Fe becomes disordered with Fe doping. The increase of the Fe–Ca peak with Fe doping in Fig. 6(c) results from the suppressed interference between the two Fe–Ca shells.

Thus we conclude the dopant Fe substitutes for Co1 in Ca_2CoO_3 block (subsystem 1). Substitution of Co1 by Fe produces electron doping. The oxygen content change might increase the carrier concentration at low Fe doping levels and electron doping becomes dominant above $x = 0.1$ resulting in the drop of carrier concentration. Chemical substitution of Fe into Ca_2CoO_3 block disorders the local structure around relative to Co at the same site. The Fe doping effect modifies the conducting CoO_2 layer as well. The structure in this layer becomes more ordered with Fe doping. The structure and carrier concentration change induced by Fe doping result in a resistivity change. The more ordered structure in the conducting CoO_2 layer suppresses the carrier scattering and increases the mobility and it plays the key role to enhance the electron transport. The highest ordered structure was achieved at $x = 0.2$ with the lowest resistivity.

Besides the structural effects, the spin-state contribution to the transport properties was investigated as well. Fig. 11(a) and (b) are the XANES spectra for Co $L_{2,3}$-edge and O K-edge for $Ca_3Co_4O_9$ and $Ca_3Co_{3.8}Fe_{0.2}O_9$. No change of the overall shape is observed for the Fe doping sample in both Co $L_{2,3}$-edge and O K-edge data. Hence there is no evident change in the multiplet structure with Fe doping. Thus no significant spin-state change occurs with Fe doping and there is no spin-state contribution to the transport property enhancement.

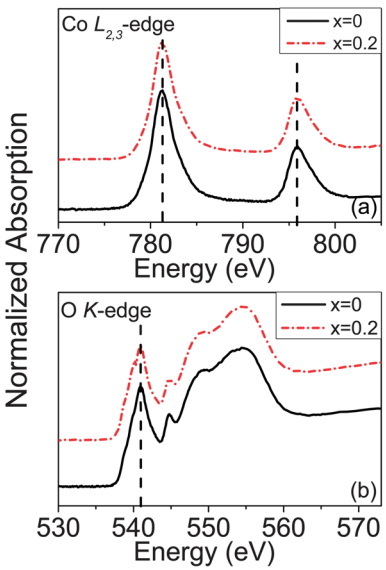

Fig. 11 XANES spectra for Co $L_{2,3}$-edge (a) and O K-edge (b) of $Ca_3Co_{4-x}Fe_xO_9$ ($x = 0$ and 0.2). Note that the overall shape of all the edges is unchanged with Fe doping.

Summary

In summary, doping with Fe significantly reduces the electrical resistivity of $Ca_3Co_4O_9$ while the Seebeck coefficient does not change much. It results in a power factor enhancement by 11% at the doping level $x = 0.2$. XRD measurements reveal that the Fe dopant enters into the structure substitutionally and modifies lattice parameters continuously with doping up to the 0.25 level studied in this work. Doping dependent Co and Fe K-edges XAFS measurements indicate that the Fe atoms substitute for the Co1 in Ca_2CoO_3 block. The valence states for Fe and Co1 were confirmed to be ~3+ and ~2+, respectively. Substitution Co1 with Fe produces electron doping. Fe doping may change the oxygen content and it probably dominates the carrier concentration at low doping levels, while electron doping becomes more important above $x = 0.1$. The local structure around Fe site becomes disordered, while the structure in the conducting CoO_2 layer is more ordered with Fe doping. The more ordered structure in the conducting CoO_2 layer increases the mobility and it plays the key role to reduce the resistivity. Thus, the highest ordered structure achieves at $x = 0.2$ with the optimized transport property. XANES spectra of $Ca_3Co_4O_9$ and $Ca_3Co_{3.8}Fe_{0.2}O_9$ on Co $L_{2,3}$-edge and O K-edge show no spin-state change with Fe doping and there is no spin contribution to the transport properties enhancement.

Acknowledgements

This work is supported by DOE Grant DE-FG02-07ER46402. The Physical Properties Measurements System was acquired under NSF MRI Grant DMR-0923032 (ARRA award). X-ray diffraction and X-ray absorption data acquisition were performed at Brookhaven National Laboratory's National Synchrotron Light Source (NSLS) which is funded by the U.S. Department of Energy. We are indebted to Prof. M. Croft of Rutgers University, for useful discussion on the structural changes accompanying doping and for providing the spectra for Fe K-edge XANES standards.

References

1 T. M. Tritt and M. A. Subramanian, *MRS Bull.*, 2006, **31**, 188–198.
2 K. Biswas, J. He, I. D. Blum, C. I. Wu, T. P. Hogan, D. N. Seidman, V. P. Dravid and M. G. Kanatzidis, *Nature*, 2012, **489**, 414–418.
3 I. Terasaki, Y. Sasago and K. Uchinokura, *Phys. Rev. B: Condens. Matter*, 1997, **56**, R12685.
4 M. Shikano and R. Funahashi, *Appl. Phys. Lett.*, 2003, **82**, 1851–1853.
5 H. Ohta, K. Sugiura and K. Koumoto, *Inorg. Chem.*, 2008, **47**, 8429–8436.
6 A. C. Masset, C. Michel, A. Maignan, M. Hervieu, O. Toulemonde, F. Studer, B. Raveau and J. Hejtmanek, *Phys. Rev. B: Condens. Matter*, 2000, **62**, 166–175.
7 S. Lambert, H. Leligny and D. Grebille, *J. Solid State Chem.*, 2001, **160**, 322–331.

8 Y. Miyazaki, M. Onoda, T. Oku, M. Kikuchi, Y. Ishii, Y. Ono, Y. Morii and T. Kajitani, *J. Phys. Soc. Jpn.*, 2002, **71**, 491.
9 H. Muguerra, D. Grebille and F. Bourée, *Acta Crystallogr., Sect. B: Struct. Sci.*, 2008, **64**, 144–153.
10 D. Grebille, S. Lambert, F. Bourée and V. Petrícek, *J. Appl. Crystallogr.*, 2004, **37**, 823–831.
11 Q. Li, *Mater. Res. Soc. Symp. Proc.*, 2006, **886**, 0886-F0801-0805.
12 H. W. Eng, P. Limelette, W. Prellier, C. Simon and R. Fresard, *Phys. Rev. B: Condens. Matter Mater. Phys.*, 2006, **73**, 033403.
13 K. Sugiura, H. Ohta, K. Nomura, M. Hirano, H. Hosono and K. Koumoto, *Appl. Phys. Lett.*, 2006, **89**, 032111.
14 B. C. Zhao, Y. P. Sun and W. H. Song, *J. Appl. Phys.*, 2006, **99**, 073906.
15 W. Wong-Ng, M. D. Vaudin, M. Otani, N. D. Lowhorn, Y. F. Hu, Q. Li and B. He, *J. Appl. Phys.*, 2007, **102**, 033520.
16 D. Kenfaui, G. Bonnefont, D. Chateigner, G. Fantozzi, M. Gomina and J. G. Noudem, *MRS Bull.*, 2010, **45**, 1240–1249.
17 G. D. Tang, H. H. Guo, T. Yang, D. W. Zhang, X. N. Xu, L. Y. Wang, Z. H. Wang, H. H. Wen, Z. D. Zhang and Y. W. Du, *Appl. Phys. Lett.*, 2011, **98**, 202109.
18 Y. H. Lin, J. Lan, Z. J. Shen, Y. H. Liu, C. W. Nan and J. F. Li, *Appl. Phys. Lett.*, 2009, **94**, 072107.
19 A. Sakai, T. Kanno, S. Yotsuhashi, A. Odagawa and H. Adachi, *Jpn. J. Appl. Phys.*, 2005, **44**, L966–L969.
20 M. Prevel, S. Lemonnier, Y. Klein, S. Hebert, D. Chateigner, B. Ouladdiaf and J. G. Noudem, *J. Appl. Phys.*, 2005, **98**, 093706.
21 Y. H. Liu, Y. H. Lin, Z. Shi, C. W. Nan and Z. J. Shen, *J. Am. Ceram. Soc.*, 2005, **88**, 1337–1340.
22 Y. F. Hu, W. D. Si, E. Sutter and Q. Li, *Appl. Phys. Lett.*, 2005, **86**, 082103.
23 H. W. Eng, W. Prellier, S. Hébert, D. Grebille, L. Méchin and B. Mercey, *J. Appl. Phys.*, 2005, **97**, 013706.
24 Y. Wang, Y. Sui, P. Ren, L. Wang, X. Wang, W. Su and H. Fan, *Chem. Mater.*, 2010, **22**, 1155–1163.
25 X. Song, Y. Chen, S. Chen, E. Barbero, E. L. Thomas and P. Barnes, *Solid State Commun.*, 2012, **152**, 1509–1512.
26 Y. Wang, L. Xu, Y. Sui, X. Wang, J. Cheng and W. Su, *Appl. Phys. Lett.*, 2010, **97**, 062114.
27 Y. Wang, Y. Sui, X. Wang, W. Su and X. Liu, *J. Appl. Phys.*, 2010, **107**, 033708.
28 Y. Wang, Y. Sui, J. Cheng, X. Wang, W. Su and H. Fan, *Appl. Phys. A: Mater. Sci. Process.*, 2010, **99**, 451–458.
29 Y. Wang, Y. Sui, X. J. Wang and W. H. Su, *J. Phys. D: Appl. Phys.*, 2009, **42**, 055010.
30 D. Li, X. Y. Qin, Y. J. Gu and J. Zhang, *J. Appl. Phys.*, 2006, **99**, 053709.
31 Q. Yao, D. L. Wang, L. D. Chen, X. Shi and M. Zhou, *J. Appl. Phys.*, 2005, **97**, 103905.
32 M. Mikami, N. Ando, E. Guilmeau and R. Funahashi, *Jpn. J. Appl. Phys.*, 2006, **45**, 4152–4158.
33 M. Mikami, K. Chong, Y. Miyazaki, T. Kajitani, T. Inoue, S. Sodeoka and R. Funahashi, *Jpn. J. Appl. Phys.*, 2006, **45**, 4131–4136.
34 T. Sun, H. H. Hng, Q. Y. Yan and J. Ma, *J. Appl. Phys.*, 2010, **108**, 083709.
35 S. Pinitsoontorn, N. Lerssongkram, N. Keawprak and V. Amornkitbamrung, *J. Mater. Sci.: Mater. Electron.*, 2011, **23**, 1050–1056.
36 C. J. Liu, L. C. Huang and J. S. Wang, *Appl. Phys. Lett.*, 2006, **89**, 204102.
37 C. J. Liu, J. L. Chen, L. C. Huang, Z. R. Lin and C. L. Chang, *J. Appl. Phys.*, 2007, **102**, 014908.
38 V. Petricek, M. Dusek and L. Palatinus, *Jana2006. The crystallographic computing system*, Institute of Physics, Praha, Czech Republic, 2006.
39 B. Ravel and M. Newville, *J. Synchrotron Radiat.*, 2005, **12**, 537–541.
40 D. C. Konningsberger and R. Prins, *X-Ray Absorption: Principles, Applications, Techniques of EXAFS, SEXAFS and XANES*, Wiley, New York, 1988.
41 T. A. Tyson, Z. Chen, Q. Jie, Q. Li and J. J. Tu, *Phys. Rev. B: Condens. Matter Mater. Phys.*, 2009, **79**, 024109.
42 Y. Miyazaki, K. Kudo, M. Akoshima, Y. Ono, Y. Koike and T. Kajitani, *Jpn. J. Appl. Phys.*, 2000, **39**, L531–L533.
43 T. Wu, T. A. Tyson, H. Chen, J. Bai, H. Wang and C. Jaye, *J. Phys.: Condens. Matter*, 2012, **24**, 455602.
44 C. D. Ling, K. Aivazian, S. Schmid and P. Jensen, *J. Solid State Chem.*, 2007, **180**, 1446–1455.
45 T. A. Tyson, T. Yu, S. J. Han, M. Croft, G. D. Gu, I. K. Dimitrov and Q. Li, *Phys. Rev. B: Condens. Matter Mater. Phys.*, 2012, **85**, 024504.
46 T. Mizokawa, L. H. Tjeng, H. J. Lin, C. T. Chen, R. Kitawaki, I. Terasaki, S. Lambert and C. Michel, *Phys. Rev. B: Condens. Matter Mater. Phys.*, 2005, **71**, 193107.
47 R. W. G. Wyckoff, *The Structure of Crystals*, Home Farm Books, 2007.
48 R. L. Blake, R. E. Hessevick, T. Zoltai and L. W. Finger, *Am. Mineral.*, 1966, **51**, 123–129.